Spatiotemporal connectivity of noise-derived seismic body waves with ocean waves and microseism excitations

Lei Li, Pierre Boué, Michel Campillo
Université Grenoble Alpes, CNRS, IRD, IFSTTAR, ISTerre, Grenoble, France
Correspondence to: Lei Li (ll.ynyf@gmail.com)

Abstract

Everywhere on the Earth planet is experiencing tiny but incessant microseisms induced by formidable natural forces, particularly, storm-driven ocean waves. Microseism noise was deemed a nuisance, but now can be turned into signals via the emerging correlation technique. We use a *P*-type phase recently derived from double-array noise correlations to study the links between global oceanic microseism sources and noise-derived seismic signals. The phase is termed P_{dmc} in this study. The two correlated seismic arrays locate in the north hemisphere, while the effective sources responsible for the construction of P_{dmc} signals lie in the south hemisphere. The temporal variations of P_{dmc} amplitudes are highly correlated with those of the power of effective sources. The P_{dmc} amplitudes are also correlated with other ineffective southern sources and anti-correlated with the northern sources. We ascribe the correlation with the ineffective southern sources to the spatiotemporal connection of the southern sources. The anti-correlation with northern sources is explained by the reverse seasonal patterns of the southern and northern sources, and that the northern sources have adverse impacts on the signal construction. A successful signal construction relies on the competition between effective and ineffective sources, not just the power of effective sources. In our case, the ocean waves in the effective source region are dominated by wind waves, whereas the excitation of microseisms is largely owing to swells by causal storms in surrounding regions.

1 Introduction

As early as the birth of seismometers in the later 19th century, the incessant background vibrations of Earth had been observed (Bernard, 1990; Dewey and Byerly, 1969; Ebeling, 2012). They were termed "microseisms" due to their feebleness. With more apparatus deployed worldwide, it was soon recognized that microseisms are ubiquitous and irrelevant to seismicity. The observation of microseisms aroused interests from various disciplines. Researchers linked the generation of microseisms to atmosphere processes and ocean wave activities. Meteorologists tried to employ land observations of microseisms to track remote oceanic storms (e.g., Harrison, 1924). To the mid-twentieth century, it has been known well that microseisms are excited by storm-driven ocean waves. The most energetic microseisms that dominate the seismic noise spectra, namely, the so-called secondary microseisms at seismic periods around 7 s (Peterson, 1993), are excited by the nonlinear interactions between nearly equal-frequency ocean waves propagating in nearly opposite directions (Hasselmann, 1963; Longuet-Higgins, 1950). The periods of the excited secondary microseisms are half those of the colliding ocean waves. By coupling the excitation theory of secondary microseisms proposed by Longuet-Higgins (1950) with the ocean wave action model, Kedar et al. (2008) modeled the secondary microseism excitations in the north Atlantic, and validated the numerical modeling by comparing with inland seismological observations. After, more authors simulated the oceanic microseism sources and some reported the consistency between predictions and observations (e.g., Ardhuin et al., 2011, 2015; Hillers et al., 2012; Nishida and Takagi, 2016; Stutzmann et al., 2012).

The seismic excitation by an oceanic microseism source has nothing special compared to that by an earthquake, in that the seismic wavefield recorded at any point is a convolution of the source time function with the Green function of the propagating medium between source and receiver. The main difference lies in the source process. The burst of earthquake leads to an impulsive source time function. Isolated seismic phases are generally distinguishable from the seismograms. In contrast, the excitation of microseisms is an incessant random process, so that the convolution mixture signals are not directly discernible. With array beamforming (Rost and Thomas, 2002) or correlation technique (Campillo and Paul, 2003; Shapiro and Campillo, 2004), specific phases from distant microseism sources have been identified from seismic noise records (e.g., Euler et al., 2014; Gerstoft et al., 2008; Landés et al., 2010; Liu et al., 2016; Meschede et al., 2017; Zhang et al., 2010). The correlation technique is advantageous in that, by correlating the noise records at two receivers, explicit seismic signals can be derived. Noise-derived surface waves have been used to infer the azimuthal and seasonal changes of noise sources (e.g., Stehly et al., 2006). Noise-derived body waves can provide better constrains in imaging the noise sources (Landés et al., 2010). Recently, deep body waves that pass through mantle and core have been constructed from ambient noise (e.g., Boué et al., 2013; Lin et al., 2013; Nishida, 2013; Poli et al., 2015; Spica et al., 2017; Xia et al., 2016). The noise-derived body waves are valuable for surveying the deep structure and for understanding the links between seismological observations and atmospheric/oceanographic phenomena.

Hillers et al. (2012) made the first systematic comparison between microseism sources derived from seismological observations and oceanographic modeling. The seismologically derived data (time resolution: 13 days; spatial resolution: 2.5° latitude × 5° longitude), are the global back-projections of near-zero-lag *P* signals generated from the cross correlations of microseism *P* waves at seismic array (Landés et al., 2010). The modeled data (time resolution: 3 hours; spatial resolution: 1° latitude × 1.25° longitude), are a global extension of the numerical simulation by Kedar et al. (2008). The two datasets are resampled to common resolutions for comparison. For the seismologically derived data, the back-projection is based on the relationship between the source-receiver distance and the horizontal slowness of teleseismic *P* wave. However, seismic phases that have common slownesses (e.g., *P* and *PP* waves), cannot be discriminated in this method (Gerstoft et al., 2008; Landés et al., 2010). Thus, the imaged sources are somewhat ambiguous. For the modeled data, coastal reflections of ocean waves, that can play a role in the ocean wave-wave interactions at near-coast regions (Ardhuin et al., 2011; Longuet-Higgins, 1950), are neglected. Due to the resonance of seismic waves in the water columns, bathymetry can have significant effect on the excitation of microseisms (Hillers et al., 2012; Kedar et al., 2008; Longuet-Higgins, 1950). The importance to account for the bathymetric effect on the microseism *P*-wave excitations has been addressed in several studies (e.g., Euler et al., 2014; Meschede et al., 2017). Hillers et al. (2012) considered the bathymetric effect, but using the amplification factors derived by Longuet-Higgins (1950) for surface waves.

There have been progress in several aspects since the study by Hillers et al. (2012). Rascle and Ardhuin (2013) published an oceanographic hindcast database that includes global oceanic secondary microseism sources (3-hour time resolution and 0.5° spatial resolution). Coastal reflections were accounted for in the modeling (Ardhuin et al., 2011). Gualtieri et al. (2014) proposed the formulae to compute the bathymetric effect on microseism body waves. Li et al. (2019) developed double-array methods that can estimate the respective slownesses of the interfering waves at two correlated seismic arrays, and thereby, provide better constrains on the ray paths of the correlated seismic phases. The double-array configuration eliminates the ambiguity in determining the source area responsible for the noise-derived signals (referred to as effective source region hereafter). In this study, we integrate these new progresses to investigate the associations of noise-derived body waves to ocean wave activities and microseism excitations. Li et al. (2019) observed a prominent *P*-type phase that originates from the interference between microseism *P* and *PKPab* waves and has no counterpart in either theoretical or real seismograms. We denote it as the P_{dmc} phase, referring to that the correlated *P* and *PKPab* waves transmit directly through the deep mantle and the outer core, respectively. In section 2 of this paper, we describe the main results on the P_{dmc} observations. In section 3, we estimate the temporal variations of the P_{dmc} signals and refute the associations to seismicity as have been reported by some authors for coda-derived core phases (e.g., Boué et al., 2014; Lin and Tsai, 2013). In section 4, we use correlation analysis to study the spatiotemporal links between the P_{dmc} signals and global oceanic microseism sources. Last, we discuss the significance of this study in seismology, oceanography and climate science.

2 Noise-derived P_{dmc} phase

Li et al. (2019) correlated the seismic noise records from two regional seismic networks at teleseismic distance: the FNET array in Japan and the LAPNET array in Finland (Fig. 1a). From the vertical-vertical components of noise correlations between the FNET-LAPNET station pairs, they observed coherent spurious arrivals (the P_{dmc} phase) that emerged ~200 s earlier than the direct *P* waves (Fig. 1b). The P_{dmc} phase has a dominant period of 6.2 s, typical for secondary microseisms. By estimating the respective slownesses of the interfering waves and their time delay, it is unveiled that a quasi-stationary phase interference between the teleseismic *P* waves at FNET and the *PKPab* waves at LAPNET, emanating from noise sources in the ocean south of New Zealand (NZ), lead to the noise-derived P_{dmc} phase (Fig. 1c). The quasi-stationary phase refers to that the interfering waves have no common path or slowness as expected by the traditional stationary phase condition, but the stack of correlation functions over a range of sources can still be constructive as an effect of finite frequency. The P_{dmc} phase has an apparent slowness of 4.6 s/deg, while the slownesses of the interfering *P* and *PKPab* waves are 4.7 s/deg and 4.2 s/deg, respectively. The observation of the P_{dmc} phase is time-asymmetric (Fig. S1a). Its absence from the mirror side is ascribed to the faintness of the corresponding source in the low-latitude Atlantic (Fig. S1b).

There are several advantages to investigate the links between noise-derived signals and microseism sources with the

P_{dmc} phase. First, the correlated *P* and *PKPab* waves are both prominent phases in the ballistic microseism wavefields. The P_{dmc} phase is easily observable from noise correlations, even between some single station pairs and on some single days (Fig. S2). Second, the isolation of P_{dmc} signals avoids potential bias caused by other prominent signals. Third, the effective source region is definite and unique. In contrast, noise-derived P wave can have multiple effective source areas (Boué et al., 2014). Fourth, the correlated FNET and LAPNET networks are next to the northern Pacific and Atlantic, respectively, while the effective source region locates in the southern Pacific. The northern oceans have consistent seasonal variation pattern distinct from (reverse to) that of the southern oceans (Hillers et al., 2012; Landés et al., 2010; Stutzmann et al., 2009). That will make the observations easier to interpret. Last, there happens to be a GEONET seismic array in NZ next to the effective source region for the P_{dmc} phase. The seismic data from GEONET provide extra support to our study.

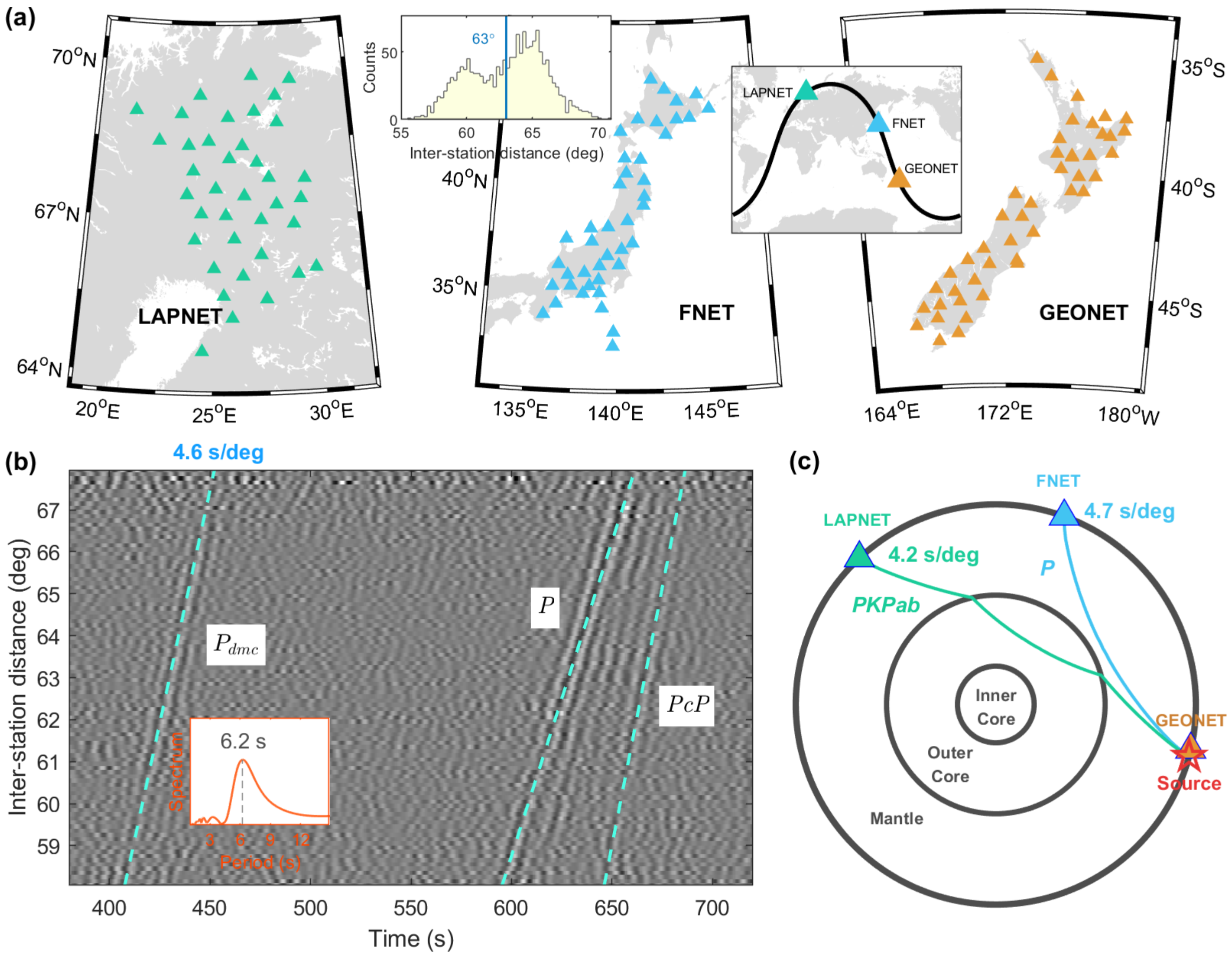

Figure 1. (a) Three regional broadband seismic networks used in this study: left, the LAPNET array in Finland (38 stations); center, the FNET array in Japan (41 stations); right, the GEONET array in New Zealand (46 stations). The histogram inset shows the distribution of the separation distances between the 1558 FNET-LAPNET station pairs. The center-to-center distance is 63° between LAPNET and FNET, and 85° between FNET and GEONET. The global inset shows the geographical locations of the three networks that are aligned on a great circle (dark line). (b) FNET-LAPNET noise correlations that are filtered between 5 s and 10 s and stacked in 0.1° bins. The spectrum inset indicates that the P_{dmc} phase has a 6.2 s peak period. (c) Ray paths of the interfering waves that generate the P_{dmc} phase. The effective source region is close to GEONET.

3 Temporal variations

We beam the daily FNET-LAPNET correlations by

$$B(t) = \langle C_{ij}(t + (d_{ij} - d_0) \cdot p) \rangle, \quad (1)$$

with $\langle\cdot\rangle$ the assemble mean operator, C_{ij} and d_{ij} the correlation function and the distance between the ith FNET station and the jth LAPNET station, d_0 the reference distance (63°), p the apparent slowness of the P_{dmc} phase (4.6 s/deg), and t the time. Figure 2 shows the envelopes of daily beams computed from the Hilbert transform of Eq. (1). The strength of daily P_{dmc} signals varies strikingly. It is extremely strong on some single days (labeled dates for instances), but indiscernible on most other days.

Considering that the region of effective source is tectonically active, one needs to investigate the plausible connection between P_{dmc} signals and seismicity. From Fig. 2, it is obvious that P_{dmc} is decorrelated with the NZ seismicity. Also, it shows no relevance with global large earthquakes as has been observed for coda-derived core phases at periods of 20 to 50 s (Boué et al., 2014; Lin and Tsai, 2013). The P_{dmc} strength exhibits a pattern of seasonal variation, which does not favor a tectonic origin (seismicity shows no clear seasonal pattern), but prefers an oceanic origin (oceanic microseism excitations have seasonal variations; see e.g. Hillers et al., 2012; Landés et al., 2010; Stehly et al., 2006; Stutzmann et al., 2009). Next, we analyze the correlations between P_{dmc} signals and oceanographic data at a global scale.

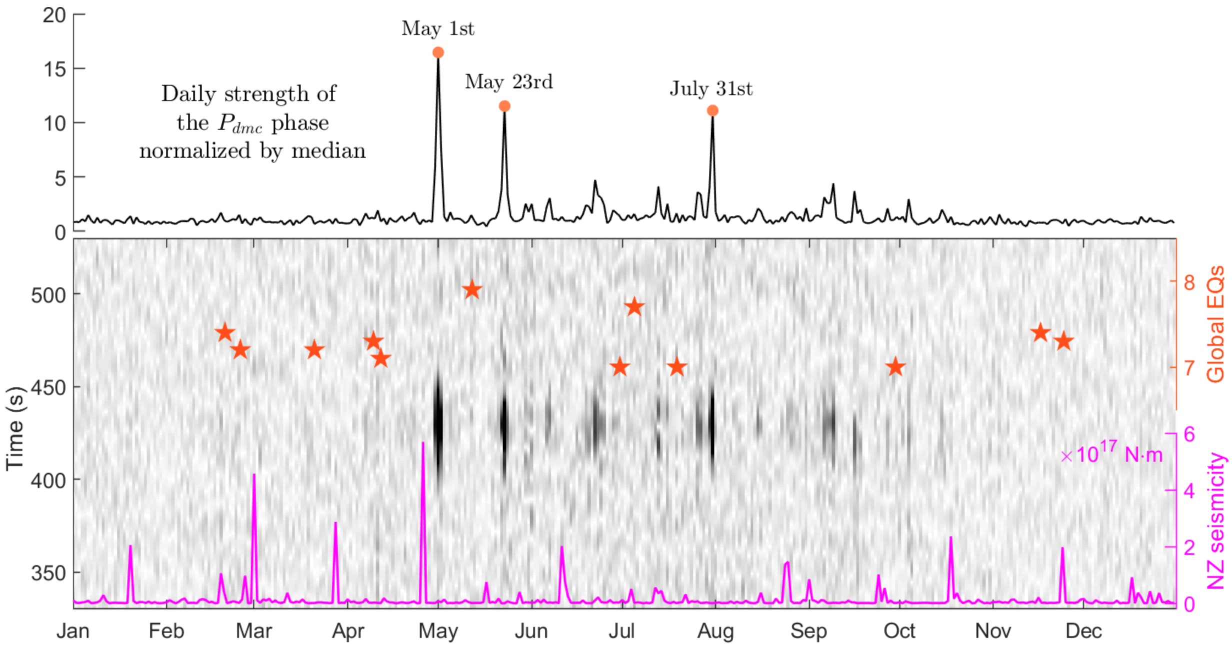

Figure 2. Temporal variations in the strength of daily P_{dmc} signals, in comparisons with daily cumulative seismic moments for magnitudes above 2.0 in NZ (line at bottom) and global large earthquakes (stars; magnitudes above 7.0). The background image is composed of columns of daily envelopes of beamed FNET-LAPNET noise correlations. Darker color represents larger amplitude. The top curve shows the daily P_{dmc} strength derived from the daily envelopes. Dates of the three largest peaks are labeled.

4 Correlation analysis

The sea state is composed of ocean waves at various frequencies and propagation directions. The nonlinear interaction between nearly equal-frequency ocean waves traveling in nearly opposite directions is equivalent to a vertical random pressure applied to the ocean surface (Hasselmann, 1963; Longuet-Higgins, 1950), so that microseisms are generated. Figure 3(a) shows a global map of average Power Spectral Density (PSD) of the equivalent surface pressure for a seismic period of 6.2 s, during the northern winter months of 2008. The most energetic microseism excitations occur in the northern Atlantic south of Greenland and Iceland (near LAPNET), and in the northern Pacific between Japan and Alaska (near FNET). Figure 3(b) shows the map for the austral winter months, with the strongest excitations occurring between NZ and Antarctic (near GEONET). The seasonal pattern of oceanic microseism excitations results from the same pattern of global wave climate (Figs 3e-f). The seasonal pattern of the P_{dmc} strength agrees with that of the microseism excitation and wave climate in the effective source region south of NZ.

We compute the correlation coefficient (denoted as r) between the P_{dmc} strength and the source PSDs at each grid point, and thereby obtain a global correlation map (Fig. 3c). As for a freedom degree of 364 for 366 samples and a p-value of 0.05 for null hypothesis, r values above 0.1 are statistically significant. The highest r arises at [47°S, 177°E] in the effective source region (E in Fig. 3c). The corresponding time series of daily source PSDs is plotted in Fig. 4, in parallel with the P_{dmc} strength. Large peaks in the P_{dmc} series have good correspondence with large peaks in the source PSD series. From Fig. 3(c), one can observe a broad region of positive r values (red colors; roughly, south Atlantic, south Pacific, and Indian ocean). However, the positive correlation does not imply a causality between the P_{dmc} phase and the sources outside the effective region E. We ascribe the apparent positive correlation to the spatial connectivity of the time-varying microseism excitation in region E with global sources (Fig. 3d). We also notice there are high-r regions that may not be fully explained by the spatial connectivity. These regions are characterized by low intensity of microseism excitations. A striking example is around [12°N, 88°E] in the Bay of Bengal (F in Fig. 3c). From Fig. 4, it can be seen that the source PSD series for [12°N, 88°E] is dominated by a single peak around May 1$^{\mathrm{st}}$, coinstantaneous with the largest P_{dmc} peak. This coincidence leads to a fake high correlation. Figures 3(g-h) show the correlation maps for h_s, which will be discussed later.

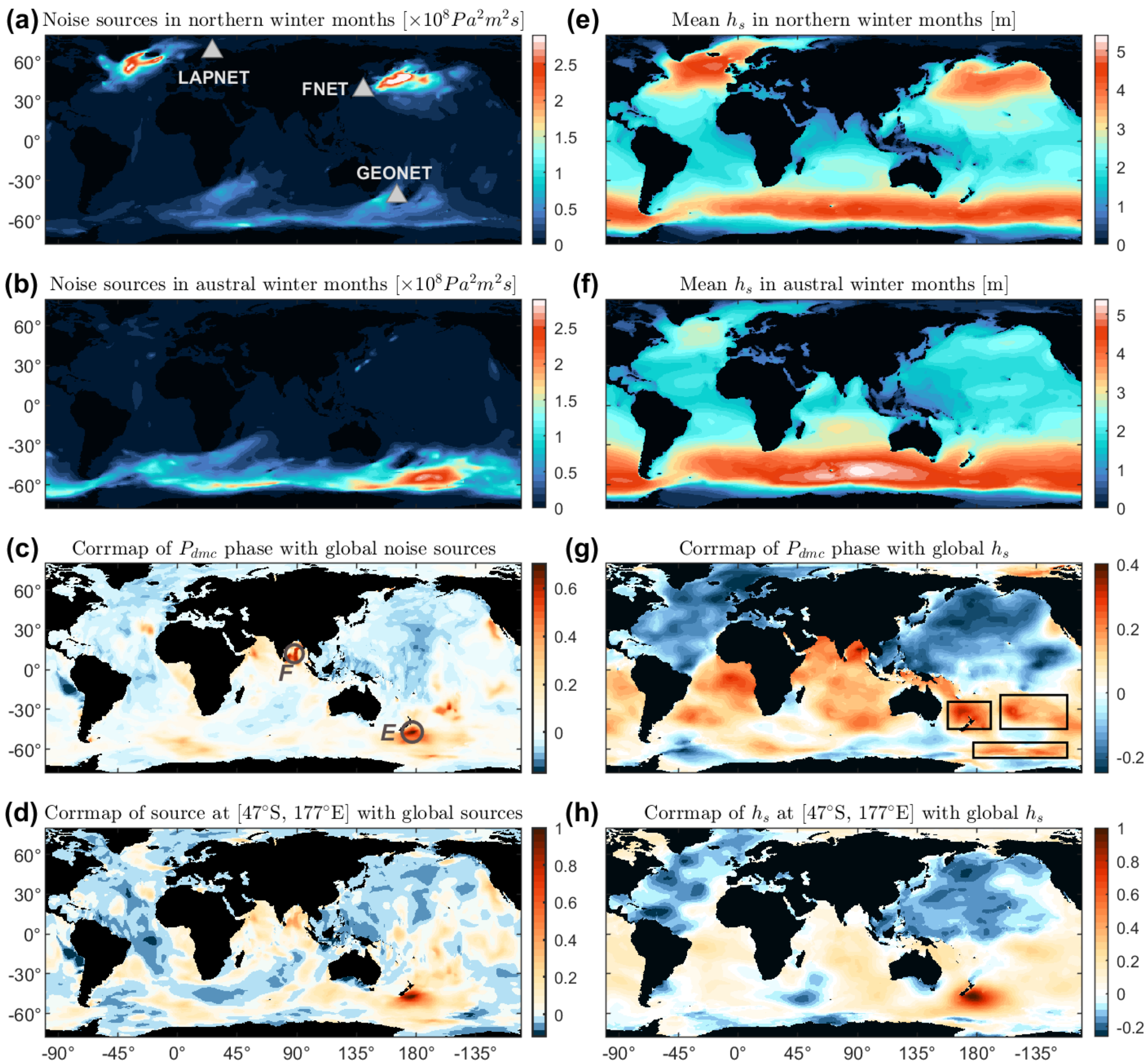

Figure 3. (a) Global map of average PSD of oceanic microseism sources in 2008 northern winter months (Jan. to Mar. and Oct. to Dec.), for a seismic perod of 6.2 s. (b) Similar to (a) but for 2008 austral winter months (Apr. to Sep.). (c) Correlation map (corrmap) for the P_{dmc} strength and global microseism sources. Circles mark two regions with highest

correlation coefficients: E, effective source region surrounding [47°S, 177°E] south of NZ; F, fake highly-correlated region surrouding [12°N, 88°E] in the Bay of Bengal. (d) Correlation map for the source at [47°S, 177°E] and global sources. (e) Mean significant wave height (h_s; four times the square root of the zeroth-order moment of ocean-wave frequency spectrum) in northern winter months. (f) Similar to (e) but for austral winter months. (g) Correlation map for the P_{dmc} strength and global wave heights. (h) Correlation map for wave heights at [47°S, 177°E] and global wave heights. The oceanographical hindcast data are provided by the IOWAGA products (Rascle and Ardhuin, 2013).

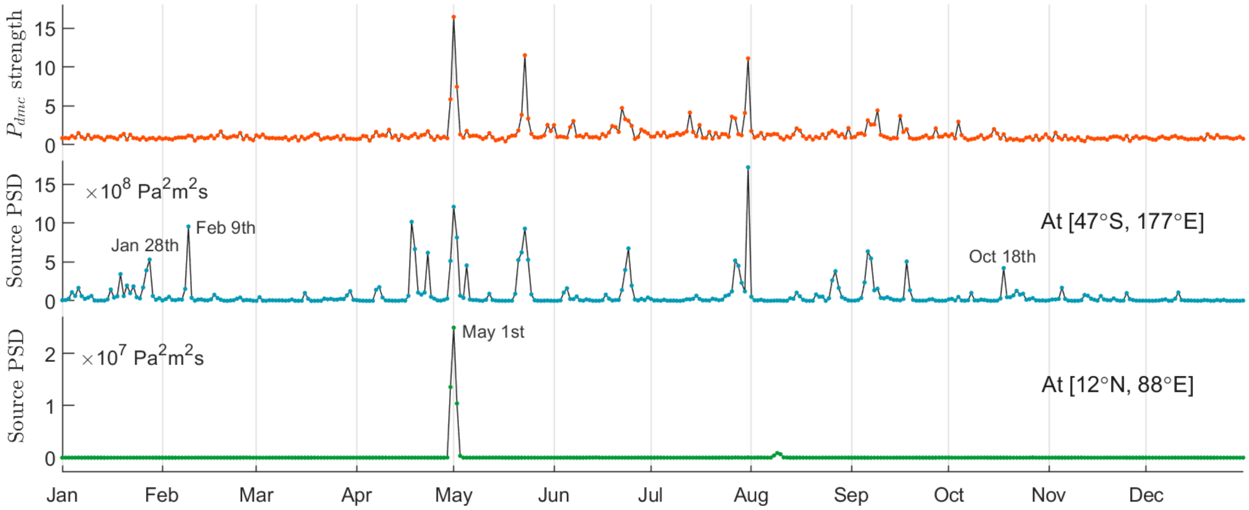

Figure 4. True correlation (r = 0.73) between the P_{dmc} strength and the source at [47°S, 177°E] in the effective source region (E in Fig. 3c), and false correlation (r = 0.71) between P_{dmc} and the source at [12°N, 88°E] in the Bay of Bengal (F in Fig. 3c).

As shown in Fig. 4, prominent peaks in the P_{dmc} series have correspondence in the source PSD series for the effective source at [47°S, 177°E]. However, there are some peaks in the latter without correspondence in the former (see the labeled dates for examples). To verify if this is due to the spreading of the effective source region has been neglected, we compare the P_{dmc} series with the source PSD series for the full effective source region, rather than at a single point. The bathymetric effect should be considered when evaluating the overall microseism excitation in the effective source region. Using the equations proposed by Gualtieri et al. (2014) and the bathymetry around NZ (Fig. 5a), we compute the bathymetric amplification factors for P waves (Fig. 5b). The P_{dmc} phase has varying sensitivities to the sources in the effective region. The weights are obtained by back-projecting the beam power of noise correlations onto a global grid (Fig. 5c; see Supplementary for technical details). Figure 5(d) shows the map of annually averaged source PSDs surrounding NZ and Fig. 5(e) shows the map after the modulation of the bathymetric amplification factors in Fig. 5(b). The spatial patterns are altered significantly, indicating the importance to account for the bathymetric effect. The final source imaging that has been weighted by Fig. 5(c), is plotted in Fig. 5(f), which agrees well with the effective source region E determined from the correlation map in Fig. 3(c). Replacing the annual PSD map in Fig. 5(d) with daily PSD maps, we obtain maps like Fig. 5(f) for each date. Averaging over the map leads to the time series of daily effective source intensity (Fig. 6). The new series has almost the same peaks as the series for [47°S, 177°E] in Fig. 4, suggesting that the observed disparities between peaks of the P_{dmc} strength and the effective source intensity are caused by other reasons.

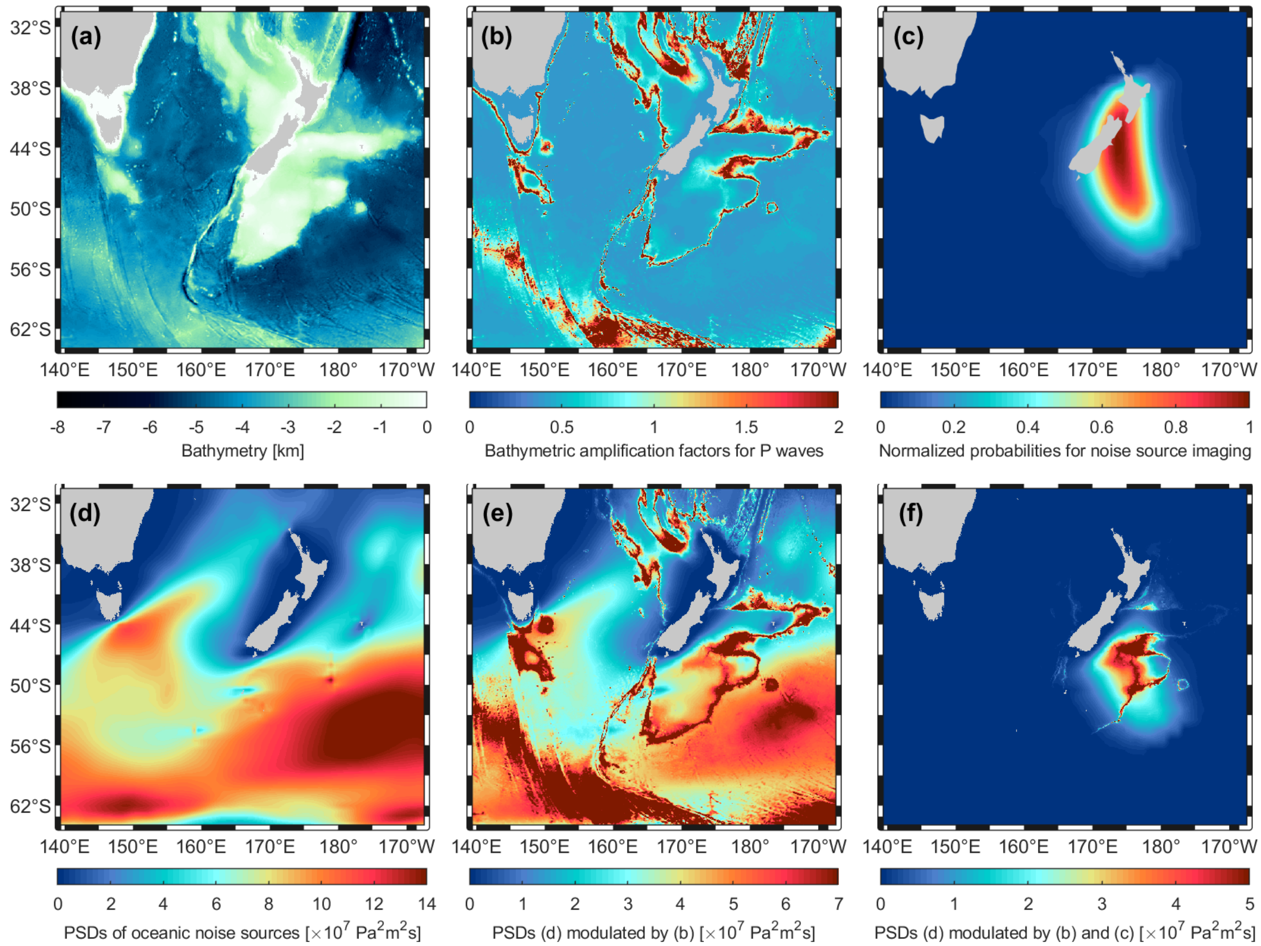

Figure 5. (a) Bathymetry around NZ. (b) Geometric average of bathymetric amplification factors for 6.2 s period *P*-type waves with slownesses of 4.2 s/deg and 4.7 s/deg. (c) Weights for oceanic microseism sources obtained from the back-projection of the FNET-LAPNET noise correlations. (d) Annual average of source PSDs in 2008. (e) Source PSDs in (d) modulated by the factors in (b). (f) Source PSDs in (e) further modulated by the weights in (c).

The microseism source PSD data are simulated from the hindcast data of ocean wave directional spectra base on the excitation theory of Longuet-Higgins (1950) and Hasselmann (1963), which have no constrains from seismological observations. One should consider the accuracy of the simulation: the peak disparities in Fig. 4 can be ascribed to the simulation error or not? The seismic noise records from the GEONET array adjacent to the effective source region provide the opportunity to validate the simulation. To obtain the daily microseism noise levels at GEONET, we apply the Hampel filter, a variant of the classic median filter, to the continuous seismograms to discard earthquakes and anomalous impulses. The filter replaces outliers with the medians of the outliers' neighbors and retains the normal samples. Technical details are provided in the Supplementary. The resultant GEONET noise level exhibits a good correlation with the effective source intensity (r = 0.7). We thus affirm that the numerical simulation is statistically reliable. When the effective source intensity is high, the GEONET noise level should also be high (see the peaks marked by dots in Fig. 6 for examples). However, due to the great spatiotemporal variability of noise sources in the effective region and the complexity of seismic waves propagating from ocean to land (Gualtieri et al., 2015; Ying et al., 2014), a larger peak in the source intensity series does not necessarily imply a larger peak in the noise level time series (e.g., comparing the peaks marked by diamonds in Fig. 6 with the beside peaks). We also emphasize that a high GEONET noise level does not need to always have a correspondence in the source intensity (see squares in Fig. 6 for example), because the GEONET stations record microseisms emanating from noise sources all around, not only from the effective source region

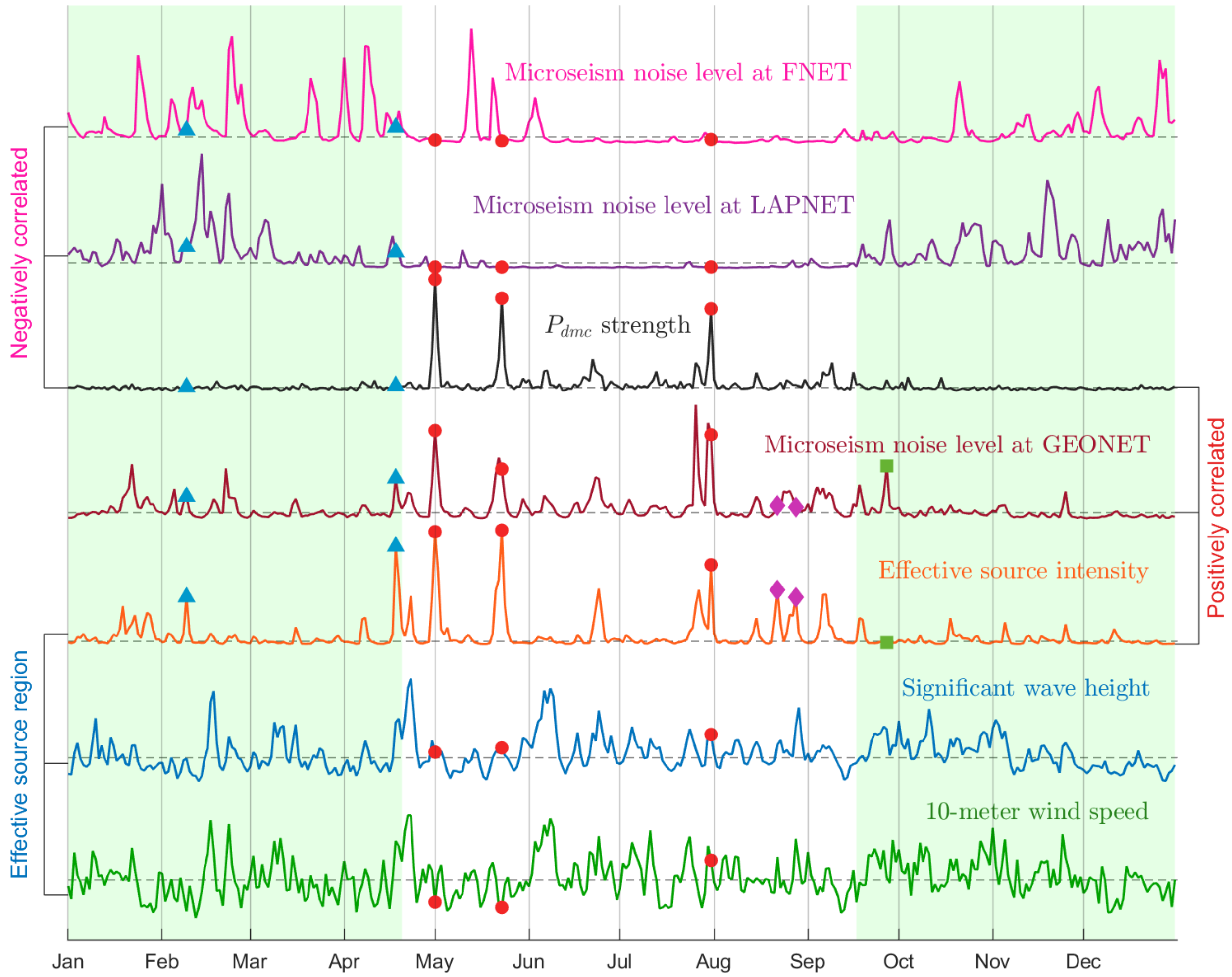

Figure 6. Temporal variations of daily P_{dmc} strength, microseism noise levels at three networks, and average wind speeds, wave heights and microseism excitations in the effective source region. The curves are normalized by their own maximums. Dashed horizontal lines denote their respective medians. Symbols mark some dates cited in the main text. When computing the effective source intensity, factors in Fig. 5(b) and weights in Fig. 5(c) are used. When computing the average wind speeds and wave heights, weights in Fig. 5(c) are used.

The above analysis validates the observed disparities between P_{dmc} strength and effective source intensity. From Fig.6, one can see that the disparities primarily emerge in the shaded period when dominant microseism sources shift to the north hemisphere. The shading roughly separates the northern winter from the austral winter. The correlation between P_{dmc} strength and effective source intensity is low in the shaded period ($r = 0.16$; outside the shading: $r = 0.74$). Large P_{dmc} peaks always emerge on dates during the austral winter when the effective source intensity is much higher than its median, and meanwhile, noise levels at FNET and LAPNET are below their respective medians (see dots in Fig. 6 for examples). The seasonal variations of oceanic sources in the south hemisphere is less strong than in the north hemisphere (Fig. 3). On some dates (see triangles in Fig. 6 for examples), the effective source intensity can be considerable, but relevant P_{dmc} peaks are still missing. We notice that the corresponding microseism levels at FNET and LAPNET are obviously above their medians. Intensive ocean activities and microseism excitations in the north Pacific and Atlantic, lead to increased microseism noise levels at FNET and LAPNET. The P_{dmc} strength is anti-correlated with microseism noise levels at FNET ($r = -0.12$) and LAPNET ($r = -0.18$). We hereby conjecture that the microseism energy from the distant effective source region is dwarfed by the energetic microseisms excited by oceanic sources closer to the correlated FNET and LAPNET arrays, and consequently, P_{dmc} signals are overwhelmed by the background noise in the FNET-LAPNET cross-correlations.

5 Discussions and conclusions

In this study, we analyzed the spatiotemporal correlations between noise-derived P_{dmc} signals and global oceanic microseism sources. In our case, the correlated seismic networks are located in the north hemisphere, while the effective source region is in the south hemisphere. Ideally, we expect a correlation map with these features: positive correlation with sources in the effective region; negative or trivial correlations with other sources. Positive correlation indicates contributing to the construction of P_{dmc} signal from noise correlations, negative correlation implies an adverse effect, and trivial correlation means a neglectable effect on the signal construction. However, we obtained a correlation map roughly showing that, the P_{dmc} signal is correlated with the southern sources and anti-correlated with the northern sources. The correlation with southern sources outside the effective region can be interpreted with the spatiotemporal connections of microseism sources in the southern oceans. The anti-correlation with northern sources can partly be explained by the reverse seasonal patterns of oceanic microseism excitations in the south and north hemispheres. Another important reason is that compared to the remote effective sources in the south hemisphere, the northern sources closer to the correlated stations have larger impacts on the microseism noise levels at stations. Strong energy flux from the northern sources outshines the microseism energy coming from the distant effective sources. That deteriorates the construction of the P_{dmc} phase. The noise-derived P_{dmc} signals are primarily observable in the austral winter. That can be, on one hand, attributed to the stronger effective source excitation during that period, and on the other hand, to the relative tranquility in the north oceans.

We generalize the above discussions to any noise-derived signal (termed as target signal for convenience). The noise correlation function is composed of the target signal, other signals and background noise. A source or a wave is called effective if it contributes to the construction of the target signal from noise correlations. Otherwise, it is called ineffective. The construction of the target signal is exclusively ascribed to the interferometry between the effective wavefields emanating from effective sources. Stronger effective sources (relative to ineffective sources) lead to a larger portion of the effective wavefields occupying in the total wavefield, and thereby, a better quality for the noise-derived target signal. Note that not all waves emanating from the effective sources, but only those following specific ray paths, are effective. In the case of the P_{dmc} phase, the effective waves are those following the paths of *P* and *PKPab*. Weak phases in the ballistic wavefield, like the PcS-PcPPcP correlation as discussed by Li et al. (2019), have fewer contributions to the noise-derived signals. Figure 7 summarizes the classification of noise sources, the decomposition of wavefields, together with the associations to the constituents of the inter-receiver noise correlation function.

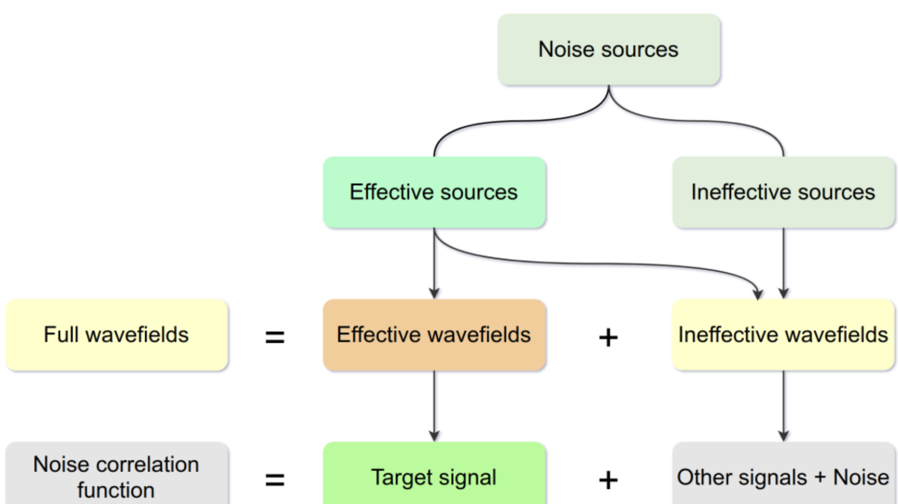

Figure 7. Sketch explanation for the relationships between noise sources and noise-derived signals.

The effective source region *E* for the P_{dmc} phase is successfully identified from the correlation map in Fig. 3(c). It is consistent with that determined from seismological back-projection (Fig. 5). The correlation map provides an easy way to identify the effective sources for noise-derived seismic signals. The double-array back-projection is superior to the classic single-array back-projection in reducing the ambiguity in the detection and location of microseism events. A catalogue of microseism events would be promising in teleseismic body-wave tomography (Boué et al., 2013; Nishida and Takagi, 2016; Zhang et al., 2010). The good consistency of the temporal variations in the P_{dmc} strength, the effective source intensity and the NZ microseism noise level (Fig. 6), provides extra supports to the analysis of the

P_{dmc} observations and the quasi-stationary phase arguments by Li et al. (2019), and also validates the numerical modeling of oceanic microseism sources by Ardhuin et al. (2011) and Rascle and Ardhuin (2013).

In the P_{dmc}-h_s correlation map in Fig. 3(g), the largest r values do not fall in region E as in Fig. 3(c), but in surrounding regions with moderate to high ocean wave activities (the bounded areas). We speculate that these regions could be the birthplaces of the colliding swells that incite the secondary microseisms in region E, or the ocean waves in these regions are driven by the same storms as the colliding waves in region E (see the spatial connectivity of h_s from Fig. 3h and supplementary movie). From Fig. 6, one can observe a high correlation between wind speed and wave height in region E ($r = 0.74$). It indicates that the ocean waves in the region E are likely dominated by the wind waves forced by local winds. The correlation between wave height and microseism excitation is low ($r = 0.25$), implying a dominant role of swells in exciting the microseisms. Extreme sea state does not guarantee strong microseism excitation. It is not surprising according to the microseism excitation theory (Hasselmann, 1963; Longuet-Higgins, 1950). In lack of equal-frequency waves coming from opposite directions, even extreme wave climate cannot incite strong secondary microseisms. In contrast, for large peaks in the microseism excitation, the corresponding wave heights are generally moderate (e.g., on May 1st and 23rd). On these two dates, the low wind speeds but moderate wave heights in region E suggest that the ocean waves are dominantly the freely travelling swells from elsewhere (see the supplementary movie). Oppositely propagating equal-frequency swells collide with each other and incite strong microseisms. Obrebski et al. (2012) reported similar observations in eastern Pacific. There are also some examples that wind waves can play a role in the excitation of microseisms (e.g., around July 31st).

We have described above the implications of this study in seismology and in understanding the process of microseism excitation. Now, we discuss the significance in oceanography and climate science. Microseisms are induced by storm-driven ocean waves (Ardhuin et al., 2015; Hasselmann, 1963; Longuet-Higgins, 1950). Seismograms have registered the imprint of climate (Aster et al., 2010; Stutzmann et al., 2009). Instrumental observation of microseisms has a history over a century, much earlier than the modern observations of ocean waves and storms. Researchers expect that past seismic records can be used to recover undocumented historical ocean storms and wave climate, which would be valuable in improving our understanding about climate change and global warming (Ebeling 2012). The correlation analysis in this study suggests that it is practicable to detect remote microseism events with land observation of microseisms. The event detection could be effective when there are no strong sources near the station, otherwise it could be missed. Stations at low latitudes where wave climate and microseism excitation are relatively mild, or inland stations far from oceans, should have better performance in remote detection. Powerful microseism excitation does not need extremal *in situ* wave height, and extremal wave climate does not necessarily produce energetic microseisms, suggesting that secondary microseism events are not perfect proxy for extremal *in situ* wave climate. However, it does not mean the long-lasting attempt to monitor remote sea state and ocean storms with land observation of secondary microseisms is unavailing. The emergence of microseism events affirms the existence of causal storms, despite the storms could be distant from the events. Last, we mention that from the correlation maps in Fig. 3, we observe an interesting phenomenon that the microseism excitations and wave climates in part of the west coast of Africa and of US in the north hemisphere are connected to those in the south hemisphere.

Acknowledgments

The seismic data of FNET, LAPNET and GEONET were provided, respectively, by the National Research Institute for Earth Science and Disaster Resilience (http://www.fnet.bosai.go.jp), the Réseau Sismologique & Géodésique Français (http://www.resif.fr) and the GEONET Data Center (https://www.geonet.org.nz). The wind hindcast data were provided by the European Centre for Medium-Range Weather Forecasts (https://www.ecmwf.int). The hindcast data of wave heights and microseism source PSDs were provided by the IOWAGA products (Rascle and Ardhuin, 2013). The bathymetry data were extracted from ETOPO1 Global Relief Model (Amante and Eakins, 2009). The computations were performed mainly on the ISTerre cluster. This work was supported by Labex OSUG@2020 (Investissements d'avenir-ANR10LABX56) and the Simone and Cino del Duca Foundation, Insitut de France.

References

Amante, C., Eakins, B.W., 2009. ETOPO1 1 Arc-Minute Global Relief Model: Procedures, Data Sources and Analysis, NOAA Technical Memorandum NESDIS NGDC-24. doi:10.7289/V5C8276M

Ardhuin, F., Gualtieri, L., Stutzmann, E., 2015. How ocean waves rock the Earth: Two mechanisms explain microseisms with periods 3 to 300s. Geophys. Res. Lett. 42, 765–772. doi:10.1002/2014GL062782

Ardhuin, F., Stutzmann, E., Schimmel, M., Mangeney, A., 2011. Ocean wave sources of seismic noise. J. Geophys. Res. Ocean. 116, 1–21. doi:10.1029/2011JC006952

Aster, R.C., McNamara, D.E., Bromirski, P.D., 2010. Global trends in extremal microseism intensity. Geophys. Res. Lett. 37, 1–5. doi:10.1029/2010GL043472

Bernard, P., 1990. Historical sketch of microseisms from past to future. Phys. Earth Planet. Inter. 63, 145–150. doi:10.1016/0031-9201(90)90013-N

Boué, P., Poli, P., Campillo, M., Pedersen, H., Briand, X., Roux, P., 2013. Teleseismic correlations of ambient seismic noise for deep global imaging of the Earth. Geophys. J. Int. 194, 844–848. doi:10.1093/gji/ggt160

Boué, P., Poli, P., Campillo, M., Roux, P., 2014. Reverberations, coda waves and ambient noise: Correlations at the global scale and retrieval of the deep phases. Earth Planet. Sci. Lett. 391, 137–145. doi:10.1016/j.epsl.2014.01.047

Campillo, M., Paul, A., 2003. Long-Range Correlations in the Diffuse Seismic Coda. Science (80-.). 299, 547–549. doi:10.1126/science.1078551

Dewey, J., Byerly, P., 1969. The early history of Seismometry (to 1900). Bull. Seismol. Soc. Am. 59, 183–227.

Ebeling, C.W., 2012. Inferring Ocean Storm Characteristics from Ambient Seismic Noise, in: Dmowska, R. (Ed.), Advances in Geophysics. Elsevier, pp. 1–33. doi:10.1016/B978-0-12-380938-4.00001-X

Euler, G.G.G., Wiens, D.D.A., Nyblade, A.A., 2014. Evidence for bathymetric control on the distribution of body wave microseism sources from temporary seismic arrays in Africa. Geophys. J. Int. 197, 1869–1883. doi:10.1093/gji/ggu105

Gerstoft, P., Shearer, P.M., Harmon, N., Zhang, J., 2008. Global P, PP, and PKP wave microseisms observed from distant storms. Geophys. Res. Lett. 35, 4–9. doi:10.1029/2008GL036111

Gualtieri, L., Stutzmann, E., Capdeville, Y., Farra, V., Mangeney, A., Morelli, A., 2015. On the shaping factors of the secondary microseismic wavefield. J. Geophys. Res. B Solid Earth 120, 6241–6262. doi:10.1029/2000GC000119

Gualtieri, L., Stutzmann, E., Farra, V., Capdeville, Y., Schimmel, M., Ardhuin, F., Morelli, A., 2014. Modelling the ocean site effect on seismic noise body waves. Geophys. J. Int. 197, 1096–1106. doi:10.1093/gji/ggu042

Harrison, E.P., 1924. Microseisms and Storm Forecasts. Nature 114, 645–645. doi:10.1038/114645b0

Hasselmann, K., 1963. A statistical analysis of the generation of microseisms. Rev. Geophys. 1, 177–210. doi:10.1029/RG001i002p00177

Hillers, G., Graham, N., Campillo, M., Kedar, S., Landès, M., Shapiro, N., 2012. Global oceanic microseism sources as seen by seismic arrays and predicted by wave action models. Geochemistry, Geophys. Geosystems 13, Q01021. doi:10.1029/2011GC003875

Kedar, S., Longuet-Higgins, M., Webb, F., Graham, N., Clayton, R., Jones, C., 2008. The origin of deep ocean microseisms in the North Atlantic Ocean. Proc. R. Soc. A Math. Phys. Eng. Sci. 464, 777–793. doi:10.1098/rspa.2007.0277

Landés, M., Hubans, F., Shapiro, N.M., Paul, A., Campillo, M., 2010. Origin of deep ocean microseisms by using teleseismic body waves. J. Geophys. Res. Solid Earth 115, 1–14. doi:10.1029/2009JB006918

Li, L., Boué, P., Campillo, M., 2019. Observation and explanation of spurious seismic signals emerging in teleseismic noise correlations. Solid Earth Discuss. 1–20. doi:10.5194/se-2019-118

Lin, F.C., Tsai, V.C., 2013. Seismic interferometry with antipodal station pairs. Geophys. Res. Lett. 40, 4609–4613. doi:10.1002/grl.50907

Lin, F.C., Tsai, V.C., Schmandt, B., Duputel, Z., Zhan, Z., 2013. Extracting seismic core phases with array interferometry. Geophys. Res. Lett. 40, 1049–1053. doi:10.1002/grl.50237

Liu, Q., Koper, K.D., Burlacu, R., Ni, S., Wang, F., Zou, C., Wei, Y., Gal, M., Reading, A.M., 2016. Source locations of teleseismic P, SV, and SH waves observed in microseisms recorded by a large aperture seismic array in China. Earth Planet. Sci. Lett. 449, 39–47. doi:10.1016/j.epsl.2016.05.035

Longuet-Higgins, M.S., 1950. A Theory of the Origin of Microseisms. Philos. Trans. R. Soc. A Math. Phys. Eng. Sci. 243, 1–35. doi:10.1098/rsta.1950.0012

Meschede, M., Stutzmann, E., Farra, V., Schimmel, M., Ardhuin, F., 2017. The Effect of Water Column Resonance on the Spectra of Secondary Microseism P Waves. J. Geophys. Res. Solid Earth 122, 8121–8142. doi:10.1002/2017JB014014

Nishida, K., 2013. Global propagation of body waves revealed by cross-correlation analysis of seismic hum. Geophys. Res. Lett. 40, 1691–1696. doi:10.1002/grl.50269

Nishida, K., Takagi, R., 2016. Teleseismic S wave microseisms. Science (80-.). 353, 919–921.

doi:10.1126/science.aaf7573
Obrebski, M.J., Ardhuin, F., Stutzmann, E., Schimmel, M., 2012. How moderate sea states can generate loud seismic noise in the deep ocean. Geophys. Res. Lett. 39, 1–6. doi:10.1029/2012GL051896
Peterson, J., 1993. Observations and Modeling of Seismic Background Noise. U.S. Geol. Surv. Open File Rep. 93-322.
Poli, P., Thomas, C., Campillo, M., Pedersen, H.A., 2015. Imaging the D″ reflector with noise correlations. Geophys. Res. Lett. 42, 60–65. doi:10.1002/2014GL062198
Rascle, N., Ardhuin, F., 2013. A global wave parameter database for geophysical applications. Part 2: Model validation with improved source term parameterization. Ocean Model. 70, 174–188. doi:10.1016/j.ocemod.2012.12.001
Rost, S., Thomas, C., 2002. Array seismology: Methods and applications. Rev. Geophys. 40, 1008. doi:10.1029/2000RG000100
Shapiro, N.M., Campillo, M., 2004. Emergence of broadband Rayleigh waves from correlations of the ambient seismic noise. Geophys. Res. Lett. 31, 8–11. doi:10.1029/2004GL019491
Spica, Z., Perton, M., Beroza, G.C., 2017. Lateral heterogeneity imaged by small-aperture ScS retrieval from the ambient seismic field. Geophys. Res. Lett. 44, 8276–8284. doi:10.1002/2017GL073230
Stehly, L., Campillo, M., Shapiro, N.M., 2006. A study of the seismic noise from its long-range correlation properties. J. Geophys. Res. 111, B10306. doi:10.1029/2005JB004237
Stutzmann, E., Ardhuin, F., Schimmel, M., Mangeney, A., Patau, G., 2012. Modelling long-term seismic noise in various environments. Geophys. J. Int. 191, 707–722. doi:10.1111/j.1365-246X.2012.05638.x
Stutzmann, E., Schimmel, M., Patau, G., Maggi, A., 2009. Global climate imprint on seismic noise. Geochemistry, Geophys. Geosystems 10, Q11004. doi:10.1029/2009GC002619
Xia, H.H., Song, X., Wang, T., 2016. Extraction of triplicated PKP phases from noise correlations. Geophys. J. Int. 205, 499–508. doi:10.1093/gji/ggw015
Ying, Y., Bean, C.J., Bromirski, P.D., 2014. Propagation of microseisms from the deep ocean to land. Geophys. Res. Lett. 41, 6374–6379. doi:10.1002/2014GL060979
Zhang, J., Gerstoft, P., Shearer, P.M., 2010. Resolving P-wave travel-time anomalies using seismic array observations of oceanic storms. Earth Planet. Sci. Lett. 292, 419–427. doi:10.1016/j.epsl.2010.02.014

Supplementary

FNET-LAPNET noise correlations

The correlation function C_{AB} between two seismograms (S_A and S_B) is given by

$$C_{AB}(\tau) = \frac{\sum_i S_A(i) S_B(i-\tau)}{\sqrt{\sum_i S_A^2(i) \sum_i S_B^2(i)}}.$$

The resultant C_{AB} consists of an acausal part and a causal part, that correspond to the negative lags ($\tau < 0$) and the positive lags ($\tau > 0$), respectively. For efficiency, it is routine to compute the correlation function with the Fast Fourier Transform:

$$C_{AB}(\tau) = \frac{\mathcal{F}^{-1}[\mathcal{F}(S_A)\mathcal{F}^*(S_B)]}{\sqrt{\sum_i S_A^2(i) \sum_i S_B^2(i)}}.$$

Figure S1(a) shows the acausal and causal sections of FNET-LAPNET noise correlations that are filtered between 5 s and 10 s and binned in distance intervals of 0.1°. The acausal section is flipped to share the time axis with the causal section. The expected locations of the acausal and causal noise sources are marked by stars on the maps of global microseism source PSDs and ocean wave heights in Fig. S1(b). The ocean wave activities and microseism excitations at the acausal source region are intense, while those in the causal source region are fainter. Consequently, the P_{dmc} phase is only observable from the acausal noise correlations.

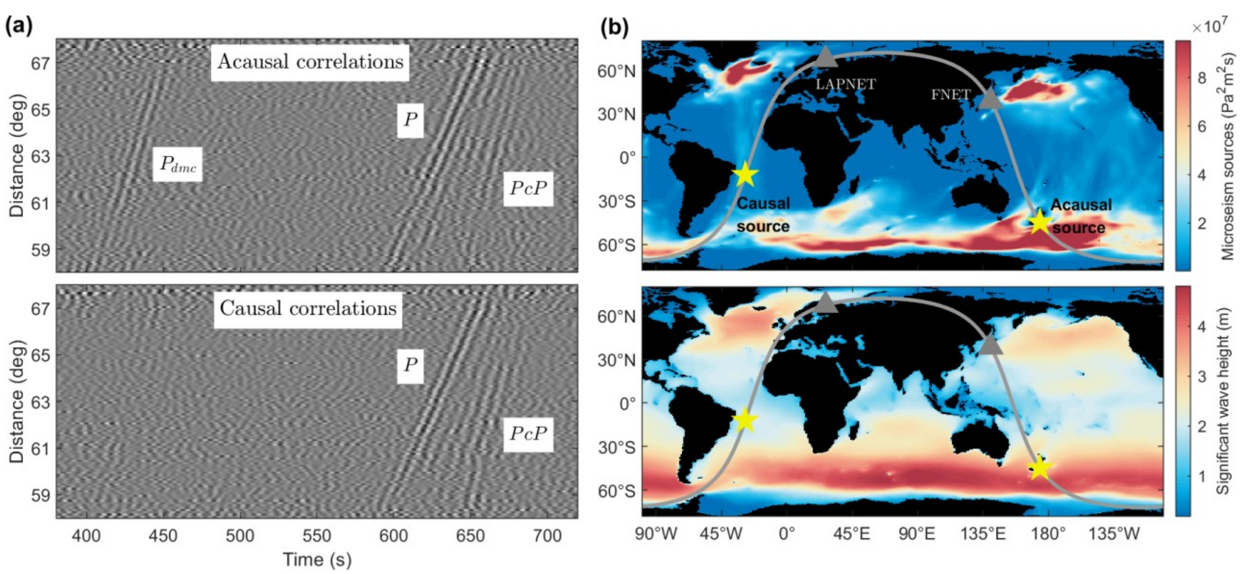

Figure S1. (a) Acausal and causal sections of FNET-LAPNET noise correlations. (b) Global maps of 6.2 s period secondary microseism sources and significant wave heights in 2008.

Noise source imaging by back-projection

Assuming the interferometry between P waves at FNET and PKPab waves at LAPNET, we image the effective noise sources through the back-projection of the FNET-LAPNET noise correlations. We beam the FNET-LAPNET noise correlations and assign the beam power

$$P_s = \langle\langle\, C_{ij}\big(t + t_{si} - t_{sj}\big)\rangle_{ij}^2\rangle_t, \qquad \text{(S1)}$$

to a 0.5° × 0.5° grid as the probabilities of noise sources on the global surface. In the above equation, $\langle\cdot\rangle_x$ means the average over x, C_{ij} is the correlation function between the *i*-th FNET station and the *j*-th LAPNET station, t_{si} is the traveltime of the P wave from the *s*-th grid point to the *i*-th FNET station, and t_{sj} is the traveltime of the PKPab waves from the *s*-th source to the *j*-th LAPNET station. The inter-station noise correlations are windowed before the beamforming (Fig. S2a). The noise source imaging for the annually stacked noise correlations is plotted in Fig. S2(c). Only the region surrounding NZ is shown. Outside the region, hardly can the P wave reach FNET or the PKPab waves reach LAPNET. Besides a well-focused imaging of the expected source region in the ocean south of NZ, we notice a secondary spot to the west. In comparisons with the power map of oceanic microseism noise sources in Fig. 5(e), we ascribe it to the strong microseism excitation in the ocean south of the Tasmania island of Australia. We also back-project the daily noise correlations on 2008-05-01 (Fig. S2b), when the P_{dmc} phase reaches the largest strength through the year (Fig. 2). As shown in Fig. S2(d), an exclusive source region is imaged, which agrees with the dominant spot in Fig. S2(c).

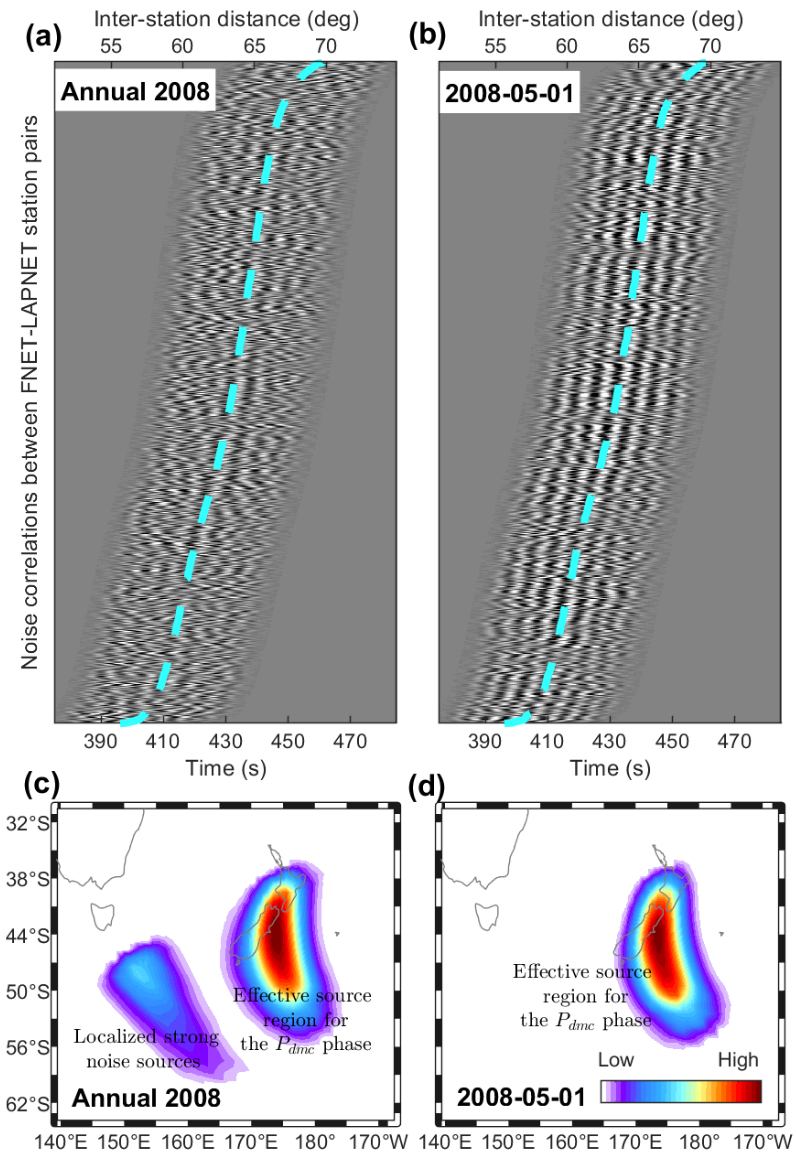

Figure S2. Inter-receiver noise correlations for all FNET-LAPNET station pairs: (a) stacked over the year of 2008; (b) on single day of 2008-05-01. The waveforms are windowed around the P_{dmc} phase. Dashed lines indicate inter-station distances. Back-projection imaging of noise sources: (c) using data from (a); (d) using data from (b).

Microseism noise levels at seismic networks

The continuous seismograms record not only the background vibrations of Earth, but also ground motions induced by seismicity or other events. Instrumental malfunction also leads to anomalous (e.g., nearly vanishing or extremely large) amplitudes in the records. These extreme amplitudes (outliers) could bias the estimates of microseism noise power. It is necessary to get rid of them from the ambient noise records before the computation of noise power. Mean and median filters are commonly-used tools for this task. However, they modify all the samples. Here, we prefer to use a variant of the median filter called Hampel filter. In contrast to the median filter that replace all samples with local medians, the Hampel filter detects outliers by compare a sample with the neighboring samples. A sample is replaced by the local median if it deviates *k* times of the median absolute deviation (MAD) from the local median, or else, it is unchanged.

We filter the vertical components of the continuous seismograms around 6.2 s period. The seismograms are then divided into 15-min segments and the power of segments are computed. We apply the Hampel filter to the time series of noise power recursively. For each sample, we compute the local median and MAD of its eight neighbors (four before and four after). A sample is replaced by the median if it deviates from the median over three times of the MAD. The de-spiked time series is resampled from a 15-min interval to a 1-hour interval, by averaging over every four samples. Then, we apply the Hampel filter again and resample the time series to a 24-hour interval. The averaging of noise levels over all stations of a seismic network leads to the time series of array noise level. Before the averaging, the Hampel filter is applied again, to discard possible anomalous values at some stations (see Fig. S3 for the example of GEONET). The final time series of microseism noise levels for networks FNET, LAPNET and GEONET are shown in Fig. 6.

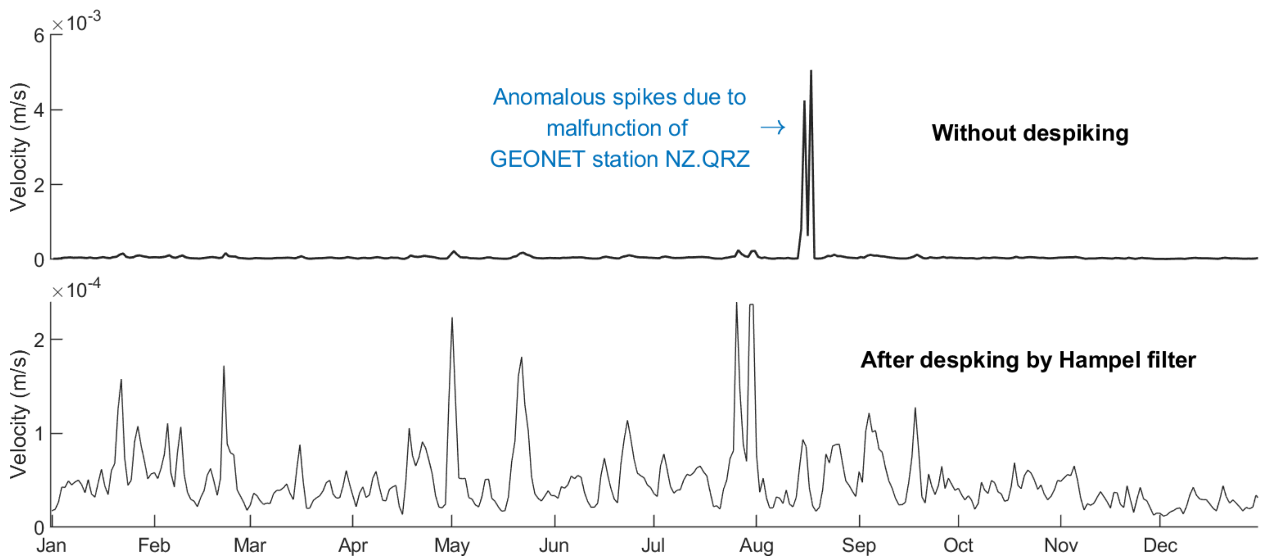

Figure S3. Comparison between the time series of daily GEONET noise levels with (lower) and without (upper) despiking using the Hampel filter.